



Impact of Thermonuclear Reaction Rate Uncertainties on the Identification of Presolar Grains from Classical Novae

Lauren Ward^{1,2} , Christian Iliadis^{1,2} , Maitrayee Bose^{3,4} , Caleb Marshall^{1,2} , Athanasios Psaltis² , and Sumner Starrfield³

¹ Department of Physics & Astronomy, University of North Carolina at Chapel Hill, NC 27599-3255, USA

² Triangle Universities Nuclear Laboratory (TUNL), Duke University, Durham, NC 27708, USA

³ Earth and Space Exploration, Arizona State University, P.O. Box 871404, Tempe, AZ 85287-6004, USA

⁴ Center for Isotope Analysis (CIA), Arizona State University, Tempe, AZ 85287-1404, USA

Received 2025 January 7; revised 2025 May 3; accepted 2025 May 4; published 2025 June 10

Abstract

Approximately 30%–40% of classical novae generate dust between 20 and 100 days following the eruption. However, there has yet to be a definitive identification of presolar stardust grains originating from classical novae. While multiple studies have suggested a nova origin for specific grains, aligning simultaneously all measured isotopic ratios of a specific grain with those predicted from simulations remains challenging. Using Monte Carlo simulations, this work investigates how uncertainties in thermonuclear reaction rates influence the isotopic ratios predicted in simulations of classical novae, specifically impacting the identification of presolar grains. In particular, we address two questions: (i) What is the impact of uncertainties in reaction rates on the range of isotopic ratios predicted by classical nova simulations? (ii) Which reaction rate uncertainties most significantly influence the predicted abundance ratios in presolar grains? Our results show that current reaction rate uncertainties affect the isotopic ratios of $^{12}\text{C}/^{13}\text{C}$, $^{14}\text{N}/^{15}\text{N}$, $^{16}\text{O}/^{17}\text{O}$, $^{16}\text{O}/^{18}\text{O}$, $^{24}\text{Mg}/^{25}\text{Mg}$, $^{24}\text{Mg}/^{26}\text{Mg}$, $^{26}\text{Al}/^{27}\text{Al}$, and $^{28}\text{Si}/^{29}\text{Si}$ by less than 20% in either carbon–oxygen or oxygen–neon (ONe) novae, especially when considering the mixing of matter throughout the entire envelope. However, the isotopic ratios of $^{28}\text{Si}/^{30}\text{Si}$, $^{32}\text{S}/^{33}\text{S}$, and $^{32}\text{S}/^{34}\text{S}$ in ONe novae are exceptions: their variability greatly exceeds a factor of 2 due to the uncertainties in the reaction rates of $^{30}\text{P}(p,\gamma)^{31}\text{S}$, $^{33}\text{S}(p,\gamma)^{34}\text{Cl}$, and $^{34}\text{S}(p,\gamma)^{35}\text{Cl}$, respectively. These results highlight the significant influence of specific reaction rates on the predicted abundance ratios and underscore the necessity for accurate nuclear measurements to reduce these uncertainties.

Unified Astronomy Thesaurus concepts: [Classical novae \(251\)](#)

1. Introduction

Primitive meteorites contain dust grains whose isotopic makeup suggests they formed from material expelled by stars, either through stellar winds or supernova ejecta (E. Zinner 2014; L. R. Nittler & F. Ciesla 2016). Following their formation, these tiny grains endured a journey through the interstellar medium, lasting approximately between hundreds of millions and one billion years, to reach the local area where the presolar cloud originated around 4.6 billion years ago. These grains withstood the mixing and evaporation processes that occurred during the solar system’s formation and were later embedded within primitive meteorites (A. G. W. Cameron 1973; R. N. Clayton et al. 1973). These so-called presolar stardust grains preserve the isotopic composition of the stellar outflows at the moment the grains condensed. Analyzing the isotopic ratios of these grains in the laboratory (E. Anders & E. Zinner 1993) serves as a powerful method for addressing questions about stellar evolution, supernovae, nucleosynthesis, mixing processes, dust formation, and the chemical evolution of the Galaxy.

Presolar stardust grains identified to date comprise diamond, silicon carbide, graphite, refractory oxides, silicates, and silicon nitride (e.g., S. Amari et al. 2014). It is believed that the majority of presolar grains originate from asymptotic giant branch stars and Type II supernovae (P. Hoppe et al. 2022).

Classical novae have also been proposed as a potential source for certain presolar grains (S. Amari et al. 2001; J. José & M. Hernanz 2007; F. Gyngard et al. 2010; J. Leitner et al. 2012; A. N. Nguyen & S. Messenger 2014; P. Haenecour et al. 2019). They occur when hydrogen-rich material is accumulated on the surface of a white dwarf within a tight binary system (for reviews, see S. Starrfield et al. 2008; J. José 2016; L. Chomiuk et al. 2021). A portion of the transferred material builds up on the white dwarf’s surface, undergoing gradual compression and heating until a thermonuclear runaway (TNR) occurs. This leads to the ejection of material into the interstellar medium at high velocities. Spectroscopy has distinguished two unique types of novae. Ejecta with a high concentration of CNO elements indicate the presence of a carbon–oxygen (CO) white dwarf (“CO novae”), whereas ejecta enriched with elements from neon to argon (in addition to CNO elements) suggest an underlying, heavier oxygen–neon (ONe) white dwarf (“ONe novae”).

Observations of classical novae across the entire electromagnetic spectrum, from radio to γ -rays (L. Chomiuk et al. 2021), offer insights for stellar explosion models, particularly concerning the energy involved and mass ejection. Elemental abundances deduced from spectroscopy of nova ejecta also yield important data, although these estimates come with considerable uncertainties (J. José & S. Shore 2008; L. N. Downen et al. 2013). Conversely, presolar stardust grains, characterized by their accurately measured isotopic ratios, serve as a potential tool for examining nova models. Classical novae are known to be abundant sources of both carbon-rich and



Original content from this work may be used under the terms of the [Creative Commons Attribution 4.0 licence](#). Any further distribution of this work must maintain attribution to the author(s) and the title of the work, journal citation and DOI.

oxygen-rich dust (R. Gehrz et al. 1998; R. D. Gehrz 2008), and as such, the isotopic makeup of these dust grains mirrors the hydrodynamic conditions and mixing events that take place during explosive nuclear burning (S. Starrfield et al. 2008).

The linkage of certain presolar grains to classical nova origins relies on unique isotopic abundance patterns. For instance, ONe novae models predict low number abundance ratios of $^{12}\text{C}/^{13}\text{C}$ and $^{14}\text{N}/^{15}\text{N}$ in comparison to solar values. Similarly, these models anticipate excess in the abundance of ^{30}Si compared to ^{29}Si (S. Amari et al. 2001; J. José et al. 2004; J. José & M. Hernanz 2007). Given that the isotopic ratios in simulated nova ejecta are more anomalous than those measured in presolar grains, it has often been presumed that the presolar grains formed after the ejecta mixed with a significantly larger fraction (over 90%) of matter with a solar composition (S. Amari et al. 2001; F. Gyngard et al. 2010; J. Leitner et al. 2012). Since there is no widespread agreement on the mechanism or source of this dilution, several authors have lately sought to align the compositions of presolar grains with predictions from nova models without necessitating any (or only a minimal degree of) dilution (C. Iliadis et al. 2018). While a nova origin has been proposed for several presolar grains (see Table 2 in C. Iliadis et al. 2018 or Table 1 in M. Bose & S. Starrfield 2019 for a list of nova candidate grains), the topic is controversial due to counter arguments that support a supernova origin for many of these grains (L. R. Nittler & P. Hoppe 2005; N. Liu et al. 2016; J. Schulte et al. 2021).

The isotopic patterns mentioned previously arise from nuclear reactions occurring during the TNR. Since the thermonuclear reaction rates operating on core matter mixed up from below are subject to uncertainties, examining their effect on simulation outcomes is crucial. Discussions on the uncertainties of reaction rates pertaining to classical novae are detailed in J. José et al. (2001, 2004), C. Iliadis et al. (2002), and M. A. van Raaij et al. (2008). However, such discussions are largely missing from the more recent studies on nova candidate grains. Recently, L. Downen et al. (2022) highlighted the significant effect of uncertainties in the $^{29}\text{Si}(p,\gamma)^{30}\text{P}$ reaction rate on the simulated $^{29}\text{Si}/^{28}\text{Si}$ ratios in nova models. This reaction was subsequently measured, and as a result, the rate uncertainties decreased by a factor of 3 at temperatures typical of novae (L. N. Downen et al. 2022). Consequently, the simulated $^{29}\text{Si}/^{28}\text{Si}$ ratios exhibit considerably less variation than seen in earlier studies.

This work aims to provide a comprehensive assessment of the effects of current uncertainties in thermonuclear reaction rates on the isotopic ratios simulated in CO and ONe novae. This information is crucial for evaluating the reliability of predicted isotopic anomalies when compared to actual observations. Additionally, our findings highlight the need for nuclear reaction measurements focused on reducing the uncertainties in rates that significantly influence important isotopic ratios. In particular, this work will provide answers to two questions: (i) What is the impact of uncertainties in reaction rates on the range of isotopic ratios predicted by classical nova simulations? (ii) Which reaction rate uncertainties most significantly influence the predicted abundance ratios in presolar grains?

The two nova models adopted in the present work are described in Section 2. The reaction network and the Monte Carlo simulation setup are presented in Section 3. Results are discussed in Section 4. A concluding summary is given in Section 5.

2. CO and ONe Classical Nova Models

The results of computer simulations are influenced by the assumptions made and the parameters selected. Some parameters are constrained by observation (e.g., the explosion energy and the elemental composition of the ejecta), while only indirect information is available for others (e.g., the rate of mass accretion from the companion, the initial composition in the burning zone, initial luminosity and mass of the white dwarf, the amount of white dwarf matter dredged up into the accreted envelope, and the effects of multicycle nova evolution). Some effects have remained nearly unexplored (e.g., the impact of magnetic fields or rotation on nova outburst). Most existing models of classical novae have been based on the assumption that the accreted matter has a solar composition, though there have been simulations of models with lower metallicity as well ($Z \gtrsim 10^{-7}$; see J. José & M. Hernanz 2007; H.-L. Chen et al. 2019).

To examine the influence of reaction rates, we will use temperature-density evolutionary paths derived from two hydrodynamical models of classical novae. We will concentrate on the hottest layer at the intersection between the white dwarf’s surface and the accreted layer, which is the location where the majority of nuclear reactions are anticipated to take place (J. José 2016).

One select model is based on S. Starrfield et al. (2020; CO novae), and another is derived from S. Starrfield et al. (2024; ONe novae). Both models accrete matter of solar composition from the companion and assume a nuclear fuel composition of 25% white dwarf and 75% solar matter. For each scenario, our simulations start close to the onset of the TNR. These models are referred to as “MDTNR”—mixing during the thermonuclear runaway—in S. Starrfield et al. (2020, 2024). Specifically, we extracted the temperature-density evolution from the CO nova model with a $1.15 M_{\odot}$ accreting white dwarf (S. Starrfield et al. 2020) and from the ONe nova model with $1.25 M_{\odot}$ (S. Starrfield et al. 2024). The maximum temperatures and densities reach $T_{\text{peak}} = 238 \text{ MK}$ and $\rho = 571 \text{ g cm}^{-3}$ in the CO nova model and $T_{\text{peak}} = 281 \text{ MK}$ and $\rho = 4704 \text{ g cm}^{-3}$ in the ONe model. The evolutionary characteristics are summarized in Table 1. For the CO white dwarf composition, we assumed 50% ^{12}C and 50% ^{16}O (see the discussion in C. Iliadis et al. 2018). The ONe white dwarf composition is adopted from C. Ritossa et al. (1996; mass point $1.17 M_{\odot}$). The initial abundances for our nucleosynthesis simulations are listed in Table 2. They represent common choices in studies of classical novae.

It is important to note that the isotopic ratios from our one-zone simulations should not be directly compared with observed values, as we do not account for convection within a burning region that consists of multiple zones, each with varying peak temperatures and densities. The advantage of the present strategy is that the simulations are fast and can be repeated many times to explore the impact of uncertainties in the nuclear reaction rates. Our Monte Carlo procedure is discussed in the next section.

3. Monte Carlo Reaction Network Simulations

We calculate the nucleosynthesis employing a reaction network that includes 213 nuclides, spanning from protons, neutrons, and ^4He to ^{55}Cr . These nuclides are interconnected through 2385 nuclear processes, such as captures of protons

Table 1
Evolutionary Characteristics of the Classical Nova Models Adopted in the Present Work

Property	CO Nova ^a	ONe Nova ^b
WD mass (M_{\odot})	1.15	1.25
WD composition	^{12}C (50%), ^{16}O (50%)	^{16}O , ^{20}Ne , ... ^d
Mixing (%) ^c	25%–75%	25%–75%
T_{peak} (MK)	238	281
ρ_{peak} (g cm^{-3})	571	4704
L_{peak} ($10^5 L_{\odot}$)	2.3	0.57
\dot{M}_{acc} ($10^{-10} M_{\odot} \text{ yr}^{-1}$)	1.6	1.6
M_{acc} ($10^{-6} M_{\odot}$)	39.0	20.0
M_{ej} ($10^{-6} M_{\odot}$)	12.8	0.067
M_{zone} ($10^{-6} M_{\odot}$) ^e	4.44	1.14

Notes.

^a From S. Starrfield et al. (2020).

^b From S. Starrfield et al. (2024).

^c The first and second percent value refer to white dwarf and solar matter, respectively. Our initial abundances are listed in Table 2.

^d From C. Ritossa et al. (1996; mass point 1.17 M_{\odot}).

^e Mass of layer with listed values of T_{peak} and ρ_{peak} extracted for present one-zone simulations.

and α particles, β decays, and reactions involving light particles, among others. The thermonuclear reaction rates employed are sourced from STARLIB version 6.10 (2022 December). This database encompasses reaction rates and their probability density functions across a temperature range from 1 MK to 10 GK, as detailed by A. L. Sallaska et al. (2013).

The probability density functions allow for the calculation of statistically significant uncertainties in reaction rates at any chosen temperature. The majority of reaction rates critical to this study, as documented in STARLIB, were determined through a Monte Carlo approach (C. Iliadis et al. 2010), which involves random sampling of all experimental nuclear physics input parameters (R. Longland et al. 2010). For some reactions relevant to classical novae, experimental rates have not yet been established, and STARLIB incorporates rate values derived from nuclear statistical model calculations performed with the TALYS code (A. Koning et al. 2023). In these instances, an assumed uncertainty factor of 10 is applied to all of such reaction rates.⁵

Stellar weak interaction rates, which depend on both temperature and density, are adopted from G. M. Fuller et al. (1982), T. Oda et al. (1994), and J.-U. Nabi & H. Klapdor-Kleingrothaus (1999). The stellar weak decay constants are tabulated at temperatures from 1 MK to 10 GK and densities from $\rho Y_e = 1$ to $10^{11} \text{ g cm}^{-3}$, where ρY_e denotes the electron mole fraction. Short-lived nuclides, e.g., ^{13}N ($T_{1/2} = 10$ minutes), ^{14}O ($T_{1/2} = 71$ s), ^{15}O ($T_{1/2} = 122$ s), ^{17}F ($T_{1/2} = 64$ s), and ^{18}F ($T_{1/2} = 110$ minutes), present at the end of a network calculation (i.e., 1 day after peak temperature), were assumed to decay to their stable daughter nuclides.

To investigate the impact of uncertainties in thermonuclear reaction rates, we conduct our analyses by simultaneously randomly sampling all rates, utilizing the rate probability densities supplied by STARLIB (C. Iliadis et al. 2015). We utilize a lognormal rate distribution for a given reaction, j , and

⁵ Specifically, we assumed $f.u. = 10$ for these reactions and sampled their rates according to Equation (2).

Table 2
Initial Abundances, by Mass, Adopted in the Present Work

Nuclide	CO Nova ^a	ONe Nova ^b
^1H	5.293E-01	5.293E-01
^2H	2.086E-05	2.086E-05
^3He	2.596E-05	2.596E-05
^4He	2.077E-01	2.077E-01
^{12}C	1.260E-01	4.548E-03
^{13}C	2.558E-05	2.558E-05
^{14}N	6.362E-04	6.362E-04
^{15}N	1.544E-06	1.544E-06
^{16}O	1.293E-01	1.333E-01
^{17}O	2.054E-06	2.054E-06
^{18}O	1.174E-05	1.174E-05
^{19}F	5.016E-07	5.016E-07
^{20}Ne	4.196E-03	7.995E-02
^{21}Ne	4.270E-06	1.499E-03
^{22}Ne	1.329E-04	1.210E-03
^{23}Na	2.769E-05	1.613E-02
^{24}Mg	4.049E-04	1.410E-02
^{25}Mg	5.363E-05	4.004E-03
^{26}Mg	6.119E-05	2.534E-03
^{27}Al	4.599E-05	2.746E-03
^{28}Si	5.375E-04	5.375E-04
^{29}Si	2.826E-05	2.826E-05
^{30}Si	1.930E-05	1.930E-05
^{31}P	5.332E-06	5.332E-06
^{32}S	2.769E-04	2.769E-04
^{33}S	2.247E-06	2.247E-06
^{34}S	1.295E-05	1.295E-05
^{35}Cl	2.922E-06	2.922E-06
^{37}Cl	9.862E-07	9.862E-07
^{36}Ar	6.199E-05	6.199E-05
^{38}Ar	1.187E-05	1.187E-05
^{39}K	2.729E-06	2.729E-06
^{41}K	2.074E-07	2.074E-07
^{40}Ca	4.622E-05	4.622E-05

Notes. Only mass fraction values in excess of $X_i = 10^{-7}$ are listed.

^a Mixed composition of 25% white dwarf matter and 75% solar matter (K. Lodders 2021) and assuming a white dwarf composition of 50% ^{12}C and 50% ^{16}O (see Table 1).

^b Mixed composition of 25% white dwarf matter and 75% solar matter (K. Lodders 2021) and adopting the white dwarf composition at mass point 1.17 M_{\odot} in C. Ritossa et al. (1996; see Table 1).

temperature, T , represented by

$$f[x(T)_j] = \frac{1}{\sigma\sqrt{2\pi}} \frac{1}{x(T)_j} e^{-[\ln x(T)_j - \mu(T)_j]^2 / [2\sigma(T)_j^2]}, \quad (1)$$

where the lognormal parameters μ and σ determine the location and the width, respectively. For a lognormal probability density, rate samples, x_i , are drawn using (R. Longland 2012)

$$x(T)_{ij} = x(T)_{\text{med},j} [f.u.(T)]_j^{p(T)_{ij}}, \quad (2)$$

where x_{med} and $f.u.$ are the median rate value and the rate factor uncertainty, respectively. Both of these are listed in columns 2 and 3 of STARLIB, respectively. The variation exponent, p_{ij} , follows a normal distribution, meaning that it is characterized by a Gaussian distribution with a mean of zero and a standard deviation of one. It is important to note that the

factor modifying the sampled reaction rate in comparison to its median value is $f.u.(T)^{p(T)}$, rather than $p(T)$. For a given network run and nuclear reaction, we sample the variation exponent exactly once, meaning $p(T)_{ij} = p_{ij}$ remains constant across all temperatures. This approach has been shown to accurately reflect the abundance uncertainties resulting from employing more intricate sampling methods (R. Longland 2012). This means that the rate samples are still temperature dependent, as can be seen from Equation (2), because of the temperature dependence of the uncertainty factor, $f.u.(T)$. Furthermore, the rates of corresponding forward and reverse reactions within a given network calculation are not sampled independently, as they adhere to the same variation exponent. The above procedure is then repeated n times to collect an ensemble of final abundance yields.

The Monte Carlo technique just described has advantages compared to varying rates one by one in sequential network runs. Estimating simulated abundances and their uncertainties can be easily achieved by using the 16th, 50th, and 84th percentiles from the resulting ensemble of final abundance yields. The influence of the uncertainty in a specific reaction rate on the outcome of the nucleosynthesis can be determined by recording the p_{ij} values for each sampled reaction network run. A scatter plot displaying the final abundance of a specific nuclide against the sampled p_{ij} values can then be analyzed to identify any correlations.

To quantify which rates have the largest impact on a specific nuclidic abundance, we will adopt the mutual information (MI) metric, which originates from information theory (E. H. Linfoot 1957; T. M. Cover & J. A. Thomas 2006). It quantifies the information one random variable conveys about another when both are sampled at the same time. For two random variables, Y and Z , with values of $\{y_1, y_2, y_3, \dots\}$ and $\{z_1, z_2, z_3, \dots\}$, respectively, their MI is defined by

$$MI = \sum_y \sum_z P(y, z) \log \left[\frac{P(y, z)}{P(y)P(z)} \right], \quad (3)$$

where $P(y)$ and $P(z)$ are marginal distributions of y and z , respectively, and $P(y, z)$ is the joint probability density. An important theorem from information theory states that the MI between two variables is zero if, and only if, the two random variables are statistically independent. MI differs from Pearson's r and Spearman's r_s coefficients in that it does not have a fixed upper limit, making its absolute value challenging to interpret directly. Nevertheless, our primary focus is on identifying the key reactions for a specific nuclide. For this objective, the relative size of the MI will be adequate.

In the following, we will discuss outcomes derived from conducting 10^4 Monte Carlo network simulations. Tests showed that this number is sufficiently large for statistical fluctuations to become much smaller than the widths of the extracted abundance distributions.

4. Results

4.1. Spreads in Isotopic Abundance Ratios Caused by Reaction Rate Uncertainties

The spreads in final isotopic abundance ratios caused by all reaction rate uncertainties are displayed in Figure 1 as “violin” plots. The distributions are the result of the Monte Carlo

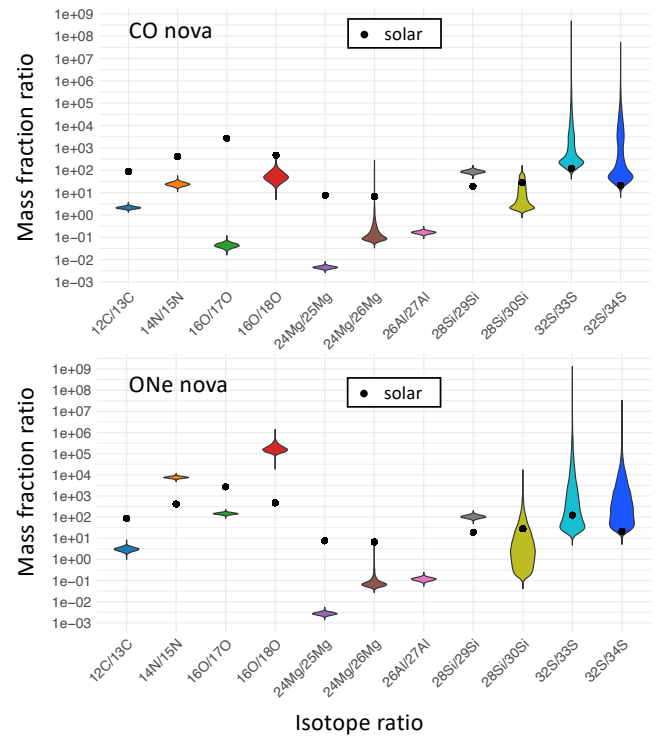


Figure 1. Violin plots of the simulated final mass fraction ratios for selected isotopes, corresponding to a time of 1 day after peak temperature. Results are obtained from one-zone Monte Carlo network calculations for (top) a CO nova model and (bottom) an ONe nova model. The black dots depict solar ratios. The shape of each distribution corresponds to the spread in the predicted isotopic ratios based solely on nuclear reaction rate uncertainties. Owing to the simplified treatment of hydrodynamics in this study, the displayed mass fraction ratios should not be directly compared to observations. Please see Section 2 for more discussion.

procedure, discussed in Section 3, and take the correlations between the individual abundances into account, i.e., each ratio sample is calculated from the same network sample. The same logarithmic y-axis is used for all ratios in each panel (top: CO nova model; bottom: ONe nova model), so that the abundance ratio uncertainties can be compared directly. The black dots represent solar ratios (K. Lodders 2021). All ratios are anomalous compared to solar values, except those for $^{28}\text{Si}/^{30}\text{Si}$, $^{32}\text{S}/^{33}\text{S}$, and $^{32}\text{S}/^{34}\text{S}$, where the spread is too large to determine whether or not they agree with solar results.

Numerical results are provided in Tables 3 and 4. They list, for each abundance pair, their solar mass fraction ratio in column (2) and the abundance ratio of the initial composition (Table 2) in column (3). The final individual median mass fractions are given in columns (4) and (5) and the median value of their ratio, $(X_a/X_b)^{\text{burn}}$, in column (6). The latter three quantities are determined from the 50th percentile of the abundance distributions. The factor uncertainty of the ratio (“factor₁”) is provided in column (7), which is obtained from $[(X_a/X_b)^{\text{high}}/(X_a/X_b)^{\text{low}}]^{1/2}$, where the high and low ratios are found from the 16th and 84th percentiles, respectively.

It can be seen that, in both nova models, the uncertainties (“factor₁”) in all ratios are less than a factor of 2, except for $^{28}\text{Si}/^{30}\text{Si}$, $^{32}\text{S}/^{33}\text{S}$, and $^{32}\text{S}/^{34}\text{S}$, where uncertainties range between factors of ≈ 3.5 and ≈ 13 .

Two-dimensional histograms of isotopic ratios are presented in Figures 2 and 3 for CO and ONe novae, respectively. Instead of mass fraction ratios, both figures present results using quantities that are standard within the meteoritics

Table 3
Simulated Isotopic Abundances (by Mass) and Corresponding Ratios From One-zone CO Nova Nucleosynthesis^a

Isotopes a, b (1)	$(X_a/X_b)^\odot$ (2)	$(X_a/X_b)^{\text{ini}}$ (3)	X_a^{burn} (4)	X_b^{burn} (5)	$(X_a/X_b)^{\text{burn}}$ (6)	Factor ₁ (7)	$(X_a/X_b)^{\text{mix}}$ (8)	Factor ₂ (9)
¹² C, ¹³ C	8.83E+01	4.92E+03	9.87E-02	4.71E-02	2.10E+00	1.13	2.61E+01	1.11
¹⁴ N, ¹⁵ N	4.12E+02	4.12E+02	8.45E-02	3.57E-03	2.36E+01	1.21	2.52E+01	1.21
¹⁶ O, ¹⁷ O	2.69E+03	6.29E+04	3.65E-04	8.55E-03	4.30E-02	1.25	1.36E+02	1.08
¹⁶ O, ¹⁸ O	4.71E+02	1.10E+04	3.65E-04	7.31E-06	5.00E+01	1.67	1.03E+04	1.03
²⁴ Mg, ²⁵ Mg	7.54E+00	7.55E+00	1.93E-07	4.31E-05	4.47E-03	1.14	6.93E+00	1.02
²⁴ Mg, ²⁶ Mg	6.62E+00	6.62E+00	1.93E-07	1.67E-06	1.13E-01	1.94	6.60E+00	1.00
²⁶ Al, ²⁷ Al	1.30E-05	7.91E-05	1.64E-01	1.16	2.63E-02	1.23
²⁸ Si, ²⁹ Si	1.90E+01	1.90E+01	1.27E-03	1.49E-05	8.58E+01	1.17	2.27E+01	1.01
²⁸ Si, ³⁰ Si	2.79E+01	2.78E+01	1.27E-03	2.83E-04	4.54E+00	3.46	1.34E+01	1.88
³² S, ³³ S	1.23E+02	1.23E+02	5.44E-04	1.31E-06	4.01E+02	5.77	1.39E+02	1.09
³² S, ³⁴ S	2.14E+01	2.14E+01	5.44E-04	3.71E-06	1.40E+02	13.0	2.47E+01	1.05

Note.

^a Column (2): solar mass fraction ratio (K. Lodders 2021); column (3): initial mass fraction ratio, calculated from Table 2; columns (4) and (5): final isotopic mass fractions 1 day after peak temperature; column (6): final mass fraction ratio—the mass fractions and their listed ratios are obtained from the 50th percentile of their frequency distributions; column (7): factor uncertainty of mass fraction ratio obtained from $[(X_a/X_b)^{\text{high}}/(X_a/X_b)^{\text{low}}]^{1/2}$, where the high and low ratios are found from the 16th and 84th percentiles, respectively; column (8): mass fraction ratio for a mixture with 1 part of processed matter with $\xi = 9$ parts of unprocessed matter in the envelope (see the text and Table 1); column (9): factor uncertainty of mixed mass fraction ratio.

Table 4
Simulated Isotopic Abundances (by Mass) and Corresponding Ratios From One-zone ONe Nova Nucleosynthesis^a

Isotopes a, b (1)	$(X_a/X_b)^\odot$ (2)	$(X_a/X_b)^{\text{ini}}$ (3)	X_a^{burn} (4)	X_b^{burn} (5)	$(X_a/X_b)^{\text{burn}}$ (6)	Factor ₁ (7)	$(X_a/X_b)^{\text{mix}}$ (8)	Factor ₂ (9)
¹² C, ¹³ C	8.83E+01	1.77E+02	3.99E-03	1.33E-03	2.99E+00	1.25	4.60E+01	1.16
¹⁴ N, ¹⁵ N	4.12E+02	4.12E+02	1.17E-01	1.56E-05	7.47E+03	1.10	3.04E+03	1.04
¹⁶ O, ¹⁷ O	2.69E+03	6.48E+04	7.84E-05	5.38E-07	1.45E+02	1.11	6.39E+04	1.01
¹⁶ O, ¹⁸ O	4.71E+02	1.13E+04	7.84E-05	4.69E-10	1.62E+05	1.43	1.13E+04	1.00
²⁴ Mg, ²⁵ Mg	7.54E+00	3.52E+00	3.70E-07	1.36E-04	2.71E-03	1.17	3.51E+00	1.00
²⁴ Mg, ²⁶ Mg	6.62E+00	5.56E+00	3.70E-07	5.33E-06	7.04E-02	1.45	5.56E+00	1.00
²⁶ Al, ²⁷ Al	3.68E-05	3.18E-04	1.16E-01	1.20	7.82E-04	1.20
²⁸ Si, ²⁹ Si	1.90E+01	1.90E+01	1.51E-02	1.46E-04	1.04E+02	1.18	3.86E+01	1.07
²⁸ Si, ³⁰ Si	2.79E+01	2.78E+01	1.51E-02	5.46E-03	2.77E+00	7.72	4.19E+00	6.20
³² S, ³³ S	1.23E+02	1.23E+02	1.01E-01	4.14E-04	2.11E+02	11.8	2.03E+02	6.77
³² S, ³⁴ S	2.14E+01	2.14E+01	1.01E-01	2.91E-04	3.07E+02	9.01	1.72E+02	3.05

Note.

^a Column (2): solar mass fraction ratio (K. Lodders 2021); column (3): initial mass fraction ratio, calculated from Table 2; columns (4) and (5): final isotopic mass fractions 1 day after peak temperature; column (6): final mass fraction ratio—the mass fractions and their listed ratios are obtained from the 50th percentile of their frequency distributions; column (7): factor uncertainty of mass fraction ratio, obtained from $[(X_a/X_b)^{\text{high}}/(X_a/X_b)^{\text{low}}]^{1/2}$, where the high and low ratios are found from the 16th and 84th percentiles, respectively; column (8): mass fraction ratio for a mixture with 1 part of processed matter with $\xi = 17$ parts of unprocessed matter in the envelope (see the text and Table 1); column (9): factor uncertainty of mixed mass fraction ratio.

community. Specifically, they present ratios of number abundances for ¹²C/¹³C, ¹⁴N/¹⁵N, ¹⁷O/¹⁶O, and ¹⁸O/¹⁶O, as well as deviations from solar matter expressed in parts per thousand⁶ for Mg, Si, and S. The vertical and horizontal dotted lines represent the solar values. The elongated shape in the silicon isotope plot is caused by the large spread of the ³⁰Si abundance (L. Downen et al. 2022). The largest spreads caused by current reaction rate uncertainties are found for $\delta^{26}\text{Mg}$, $\delta^{30}\text{Si}$, $\delta^{33}\text{S}$, and $\delta^{34}\text{S}$, and in particular, it cannot be determined whether or not these ratios obtained from our one-zone simulations are consistent with solar values.

4.2. Effects of Mixing across the Envelope

We have considered so far only the nucleosynthesis in the hottest zone of the accreted envelope, where most of the

nucleosynthesis is taking place. The mass of the burning zone, which is given in the last row of Table 1, represents 11% and 6% of the total envelope mass in the CO and ONe model, respectively. A hydrodynamic model takes into account the onset and extension of convective transport throughout the envelope, ranging from the largest peak temperatures near the white dwarf surface to the lowest peak temperatures in the outer envelope. Convection has the important effect of transporting fragile isotopes to cooler layers, where they are more likely to survive their destruction by nuclear reactions, as well as of providing the hottest zones, where most of the nucleosynthesis occurs, with fresh hydrogen fuel. For about 5–10 minutes before peak temperature is reached, the envelope is fully convective. Convection then recedes from the surface during the expansion of the envelope, so that the composition of the envelope at the time of matter ejection is never homogeneous. For details, see J. José (2016).

⁶ The delta values are defined as $\delta^i Y \equiv \delta^i Y = [(^i Y / Y) / (^i Y / Y)^\odot - 1] \times 1000$, where Y denotes the number abundance.

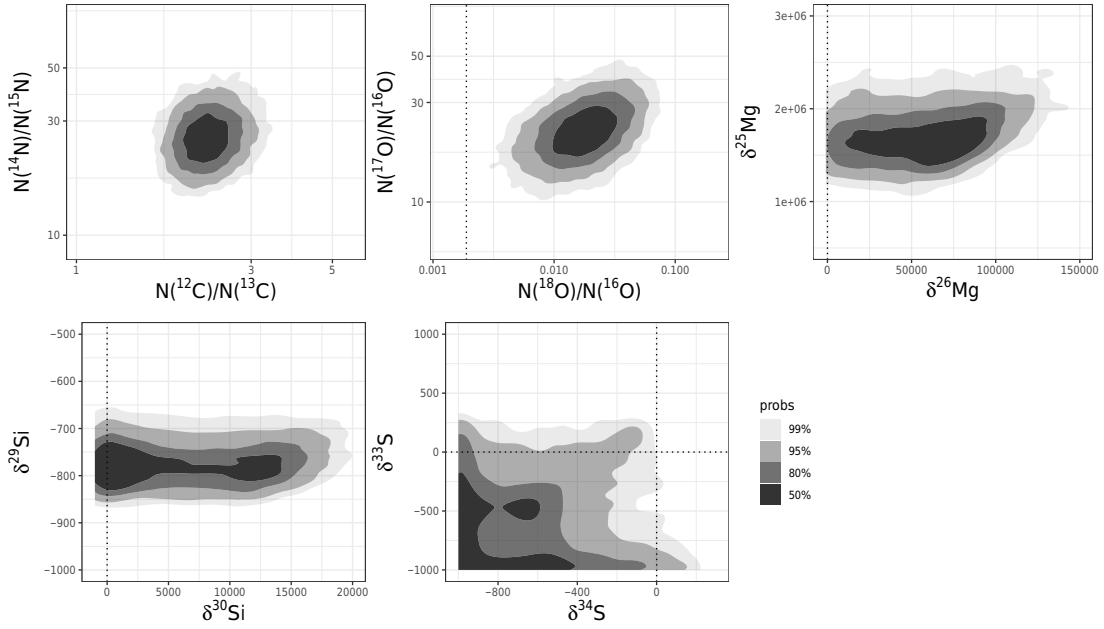


Figure 2. Two-dimensional histograms of the simulated final isotopic ratios for the CO nova model. The gray shaded areas depict regions of probability, from 50% (darkest) to 99% (lightest). The vertical and horizontal dotted lines indicate solar values. Please see the caveat in Figure 1 for a comparison of these mass fraction ratios with observations.

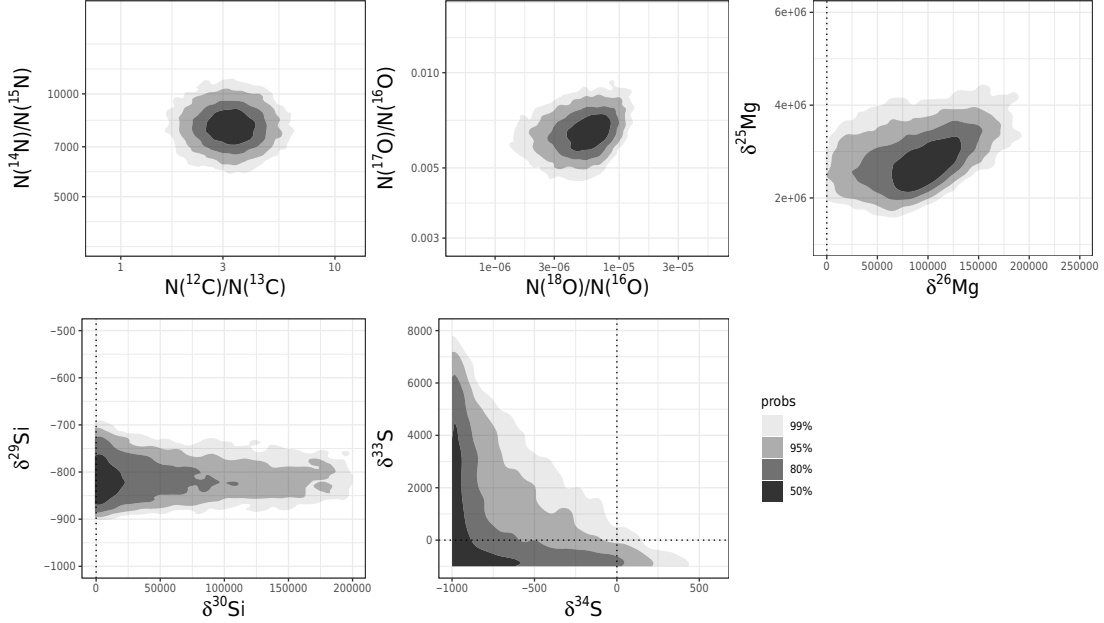


Figure 3. Two-dimensional histograms of the simulated final isotopic ratios for the ONe nova model. The gray shaded areas depict regions of probability, from 50% (darkest) to 99% (lightest). The vertical and horizontal dotted lines indicate solar values. Please see the caveat in Figure 1 for a comparison of these mass fraction ratios with observations.

Presolar grains are likely to condense in localized regions of the ejecta from material that underwent convection between different burning zones. Any mixing of matter between the hottest zone and those that achieve lower peak temperatures (and thus less nuclear processing) is expected to reduce the spread in the simulated isotopic ratios. Therefore, relatively large uncertainties obtained from the hottest burning zone (column (7) in Tables 3 and 4) may be significantly reduced in the mixed envelope.

To investigate the approximate effects of this mixing, while considering that we are mainly interested in the nuclear uncertainties of isotopic abundance ratios, we applied a simple

prescription. We computed the mass fraction ratios in matter representing a mixture with one part of processed matter (i.e., our final simulated abundance ratios for a single burning zone) and ξ parts of unprocessed matter (i.e., the initial mass fractions listed in Table 2) from

$$(X_a/X_b)^{\text{mix}} = \frac{X_a^{\text{burn}} + \xi X_a^{\text{ini}}}{X_b^{\text{burn}} + \xi X_b^{\text{ini}}}, \quad (4)$$

where $(X_a/X_b)^{\text{mix}}$ is the isotopic abundance ratio in the mixed composition and $\xi = M_{\text{acc}}/M_{\text{zone}}$ (Table 1). It must be emphasized that, since we are disregarding any other burning

zones, the values calculated from Equation (4) represent an extreme estimate. We expect that the actual values are in the range between the one-burning zone result, $(X_a/X_b)^{\text{burn}}$ (column (6) in Tables 3 and 4), and the mixed-matter estimate, $(X_a/X_b)^{\text{mix}}$ (column (8)).

This assumption holds whenever the abundance of a specific isotope decreases during thermonuclear burning, regardless of whether it occurs in the hottest zone or any other zone. In this scenario, the second term in the numerator or denominator of Equation (4) dominates over the first, reducing any spread in the abundance, X_b^{burn} . Our assumption also remains valid when the abundance increases across all burning zones. Since thermonuclear reaction rates are highly temperature sensitive, the greatest increase will occur in the hottest zone—the focus of this study. However, the assumption may break down if the outer layers enhance the final abundance while the deepest zone does not. Investigating this secondary effect lies beyond the scope of the present work.

The factor uncertainties of the mixed abundance ratios (“factor₂”) are listed in column (9) of Tables 3 and 4. Generally, the uncertainties are considerably diminished when compared to those derived under the single burning zone assumption (see column (7)), albeit with some notable exceptions. Specifically, in the context of the CO nova model, the uncertainties noted in column (9) are less than a factor of 1.2, with the exception of the $^{28}\text{Si}/^{30}\text{Si}$ ratio, where we find factor₂ ≈ 1.6 . However, such a level of uncertainty can be considered relatively modest. In the ONe nova model, uncertainties for all isotopic ratios are less than factor₂ ≈ 1.2 , except for $^{28}\text{Si}/^{30}\text{Si}$, $^{32}\text{S}/^{33}\text{S}$, and $^{32}\text{S}/^{34}\text{S}$. In the latter cases, significantly larger uncertainties are obtained (factor₂ ≈ 3 –7), even when considering a mixed composition.

The variance in behavior of these three isotopic ratios between CO and ONe novae can be traced back to Equation (4). In CO novae, the peak temperature (Table 1) is too low to facilitate significant production of ^{30}Si , ^{33}S , or ^{34}S . Consequently, the denominator in Equation (4) is predominantly influenced by the initial abundance of these isotopes (X_b^{ini}), leading to minimal uncertainty in the ratio $(X_a/X_b)^{\text{mix}}$. Conversely, in ONe novae, the higher peak temperature is sufficient to cause a net production of these three isotopes, making the denominator in Equation (4) largely dependent on the term representing burned matter (X_b^{burn}). This gives rise to significantly greater uncertainties in the isotopic ratio, $(X_a/X_b)^{\text{mix}}$.

As already mentioned above, the spreads of the final isotopic abundance ratios result from the simultaneous sampling of all reaction rates. We will next examine which reaction rate uncertainties are most responsible for the isotopic abundance ratio spreads.

4.3. Correlations between Isotopic Abundance Ratios and Reaction Rates

We computed the MI metric for 213 isotopes \times 2385 reactions, subsequently ranking the results by their impact in a descending order based on the MI values. Table 5 presents a summary of strong correlations between the final (unmixed) abundance ratio, $(X_a/X_b)^{\text{burn}}$, versus sampled reaction rate (see Section 3) for both nova models, focusing exclusively on reactions that exhibit a MI value exceeding ≈ 0.3 . Upon visually examining the correlation plots, it was found that MI values lower than this threshold are indicative of only weak

Table 5

Reactions with the Greatest Impact on Isotopic Ratios due to Uncertainties in Their Rates

Ratio	CO Nova Model		ONe Nova Model	
	Reaction	MI	Reaction	MI
$^{12}\text{C}/^{13}\text{C}$	$^{13}\text{N}(p,\gamma)^{14}\text{O}$	0.71	$^{13}\text{C}(p,\gamma)^{14}\text{N}$	0.78
$^{14}\text{N}/^{15}\text{N}$	$^{15}\text{N}(p,\alpha)^{12}\text{C}$	1.4	$^{14}\text{N}(p,\gamma)^{15}\text{O}$	1.5
$^{16}\text{O}/^{17}\text{O}$	$^{16}\text{O}(p,\gamma)^{17}\text{F}$	0.37	$^{17}\text{O}(p,\alpha)^{14}\text{N}$	0.95
$^{16}\text{O}/^{18}\text{O}$	$^{18}\text{F}(p,\alpha)^{15}\text{O}$	0.78	$^{18}\text{F}(p,\alpha)^{15}\text{O}$	1.0
$^{24}\text{Mg}/^{25}\text{Mg}$	$^{24}\text{Mg}(p,\gamma)^{25}\text{Al}$	0.67	$^{24}\text{Mg}(p,\gamma)^{25}\text{Al}$	0.56
$^{24}\text{Mg}/^{26}\text{Mg}$	$^{26}\text{Al}^m(p,\gamma)^{27}\text{Si}$	1.2	$^{26}\text{Al}^m(p,\gamma)^{27}\text{Si}$	0.66
$^{26}\text{Al}/^{27}\text{Al}$	$^{26}\text{Al}^s(p,\gamma)^{27}\text{Si}$	0.85	$^{26}\text{Al}^s(p,\gamma)^{27}\text{Si}$	0.86
$^{28}\text{Si}/^{29}\text{Si}$	$^{29}\text{Si}(p,\gamma)^{30}\text{P}$	0.43	$^{29}\text{Si}(p,\gamma)^{30}\text{P}$	0.48
	$^{28}\text{Si}(p,\gamma)^{29}\text{P}$	0.29	$^{28}\text{Si}(p,\gamma)^{29}\text{P}$	0.25
$^{28}\text{Si}/^{30}\text{Si}$	$^{30}\text{P}(p,\gamma)^{31}\text{S}$	1.6	$^{30}\text{P}(p,\gamma)^{31}\text{S}$	1.9
$^{32}\text{S}/^{33}\text{S}$	$^{33}\text{S}(p,\gamma)^{34}\text{Cl}$	1.5	$^{33}\text{S}(p,\gamma)^{34}\text{Cl}$	1.7
$^{32}\text{S}/^{34}\text{S}$	$^{34}\text{S}(p,\gamma)^{35}\text{Cl}$	1.4	$^{34}\text{S}(p,\gamma)^{35}\text{Cl}$	1.2

Note.

^a Only reactions with strong correlations, i.e., $\text{MI} \geq 0.3$, are listed (see the text).

correlations, as evidenced by nearly symmetric configurations within the plots (see Section 3). Examples of strong correlations between the final abundance ratio, $(X_a/X_b)^{\text{burn}}$, versus sampled reaction rate (see Section 3) are presented in Figure 4. All three panels are obtained for the ONe nova model.

The correlation of the final $^{28}\text{Si}/^{30}\text{Si}$ abundance ratio with the $^{30}\text{P}(p,\gamma)^{31}\text{S}$ reaction rate ($\text{MI} = 1.9$) is depicted in the first panel. The impact of this rate on nova nucleosynthesis has been pointed out by J. José et al. (2001), C. Iliadis et al. (2002), and C. Wrede (2014). Although nuclear structure information relevant for this reaction has been obtained experimentally (A. Parikh et al. 2011; D. Irvine et al. 2013; M. B. Bennett et al. 2016; A. Kankainen et al. 2017; K. Setoodehnia et al. 2020; T. Budner et al. 2022; M. Kamil et al. 2022) as well as theoretically (B. A. Brown et al. 2014), large uncertainties remain in its thermonuclear rate.

The second panel presents the strong correlation of the $^{32}\text{Si}/^{33}\text{S}$ abundance ratio with the $^{33}\text{S}(p,\gamma)^{34}\text{Cl}$ ($\text{MI} = 1.7$) reaction rate. This rate has been estimated directly by J. Fallis et al. (2013) and indirectly by A. Parikh et al. (2014), who report a spread in the total rate by several orders of magnitude and a factor of ≈ 5 , respectively, at a temperature of 100 MK. The cause of the uncertainties are ambiguous spin-parity assignments of unobserved resonances near a center-of-mass energy of ≈ 200 keV.

The correlation of the $^{32}\text{Si}/^{34}\text{S}$ abundance ratio with the $^{34}\text{S}(p,\gamma)^{35}\text{Cl}$ ($\text{MI} = 1.2$) reaction rate is depicted in the third panel. This rate was recently investigated. The level structure of ^{35}Cl , especially near the proton threshold, was measured by S. A. Gillespie et al. (2017) and K. Setoodehnia et al. (2019). It was found that the spectroscopic factors of the low-energy resonances are small (on the order of $\approx 1\%$) and that several levels have ambiguous spin-parity assignments. The direct inverse-kinematics measurement of M. Lovely et al. (2021) obtained resonance strengths down to ≈ 270 keV center-of-mass resonance energy, but some of their results are in poor agreement both with previous direct normal-kinematics (P. Endt 1990) and indirect transfer experiments (S. A. Gillespie et al. 2017). The rate presented in

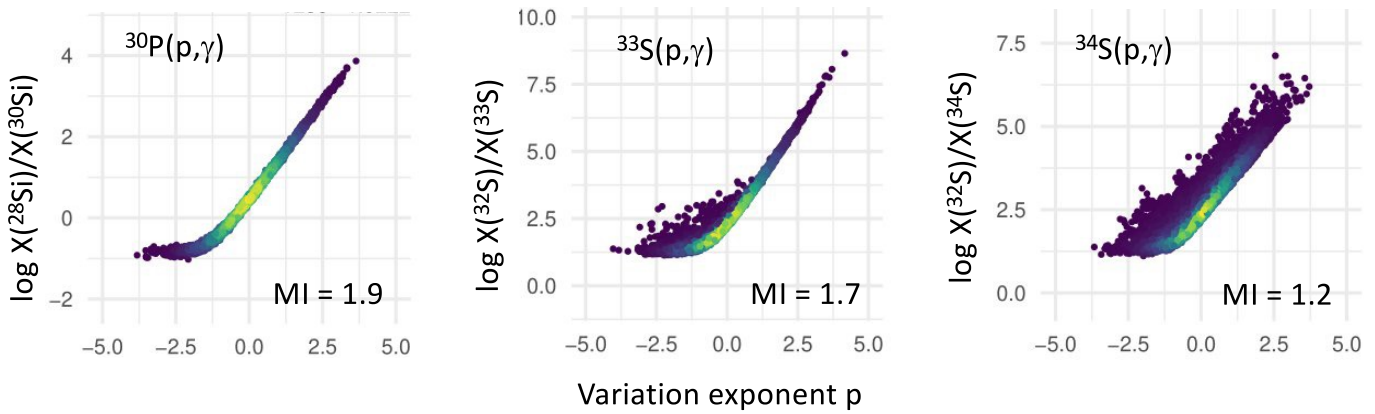


Figure 4. Correlations of the simulated final abundance ratio, $(X_a/X_b)^{\text{burn}}$, with the variation exponent, p , of a given reaction; see Equation (2). Values for the MI are also given. The results are obtained for the same simulations that gave rise to Figures 1, 2, and 3. The ordinate shows the logarithm of the mass fraction ratio. (Left) $^{28}\text{Si}/^{30}\text{Si}$ ratio vs. $^{30}\text{P}(p, \gamma)^{31}\text{S}$ rate; (middle) $^{32}\text{S}/^{33}\text{S}$ ratio vs. $^{33}\text{S}(p, \gamma)^{34}\text{Cl}$ rate; (right) $^{32}\text{S}/^{34}\text{S}$ ratio vs. $^{34}\text{S}(p, \gamma)^{35}\text{Cl}$ rate. All panels refer to the ONe nova model.

W. A. Richter et al. (2020) is entirely based on shell-model calculations and, therefore, is subject to large uncertainties.

Given the lack of a comprehensive evaluation for the three reaction rates mentioned, STARLIB has adopted an uncertainty factor of 10 for these at all temperatures (Section 3).

5. Summary

Classical novae are prolific dust producers, and it has long been thought that isotopes synthesized during the explosion will find their way into presolar stardust grains that are found in primitive meteorites. The identification of such presolar grains would place important constraints on numerical models of classical novae. While a nova origin has been proposed for several presolar grains, the topic is controversial due to counterarguments that support a supernova origin for many of these grains.

This work was motivated by the origin of presolar stardust grains from classical novae and the complexities in identifying such grains by analyzing isotopic ratios. By using Monte Carlo nucleosynthesis simulations of CO and ONe nova models, we explored how thermonuclear reaction rate uncertainties affect the prediction of isotopic ratios in classical novae. This information is crucial for connecting isotopic measurements in presolar grains with theoretical models of novae. Our nucleosynthesis simulations utilized the STARLIB database of reaction rates, which includes rate uncertainties and probability densities for all nuclear reactions of interest. Our detailed simulations were performed for the hottest zone in the CO and ONe nova models, and we investigated how the processed isotopic ratios and their associated uncertainties change after mixing with cooler outer layers that experienced little nucleosynthesis.

The main results of the present work are summarized as follows:

- If grains condense exclusively from matter processed in the hottest zone, thermonuclear reaction rate uncertainties give rise to variations in $^{28}\text{Si}/^{30}\text{Si}$, $^{32}\text{S}/^{33}\text{S}$, and $^{32}\text{S}/^{34}\text{S}$, for both CO and ONe nova models explored here, between factors of ≈ 2 and 13 (see “factor₁” in Tables 3 and 4). The ratios for $^{12}\text{C}/^{13}\text{C}$, $^{14}\text{N}/^{15}\text{N}$, $^{16}\text{O}/^{17}\text{O}$, $^{16}\text{O}/^{18}\text{O}$, $^{24}\text{Mg}/^{25}\text{Mg}$, $^{26}\text{Al}/^{27}\text{Al}$, and $^{28}\text{Si}/^{29}\text{Si}$ vary by less than a factor of ≈ 2 .

- When mixing between the hottest zone and nearly unprocessed matter of the envelope is taken into account (see “factor₂” in Tables 3 and 4), the abundance ratio variations generally become smaller. For CO novae, only the $^{28}\text{Si}/^{30}\text{Si}$ ratio varies by more than a factor of ≈ 1.5 . For ONe novae, the $^{28}\text{Si}/^{30}\text{Si}$, $^{32}\text{S}/^{33}\text{S}$, and $^{32}\text{S}/^{34}\text{S}$ ratios vary by factors between ≈ 3 and 7.
- The most important rate uncertainties affecting the variations in the $^{28}\text{Si}/^{30}\text{Si}$, $^{32}\text{S}/^{33}\text{S}$, and $^{32}\text{S}/^{34}\text{S}$ abundance ratios are caused by the $^{30}\text{P}(p, \gamma)^{31}\text{S}$, $^{33}\text{S}(p, \gamma)^{34}\text{Cl}$, and $^{34}\text{S}(p, \gamma)^{35}\text{Cl}$ reactions, respectively (see Table 5 and Figure 4).

To enhance the predictive accuracy of nova models concerning isotopic anomalies observed in presolar grains, nuclear reaction measurements to minimize these rate uncertainties are crucial. The present work provides renewed interest in additional measurements of several reactions.

Acknowledgments

We would like to thank the anonymous reviewer for the helpful suggestions. We would also like to thank Jordi José and Richard Longland for the valuable feedback. This work was supported in part by the DOE, Office of Science, Office of Nuclear Physics, under grants DE-FG02-97ER41041 (UNC) and DE-FG02-97ER41033 (TUNL).

ORCID iDs

Lauren Ward <https://orcid.org/0000-0002-7948-3345>
 Christian Iliadis <https://orcid.org/0000-0003-2381-0412>
 Maitrayee Bose <https://orcid.org/0000-0002-7978-6370>
 Caleb Marshall <https://orcid.org/0000-0002-1194-2920>
 Athanasios Psaltis <https://orcid.org/0000-0003-2197-0797>
 Sumner Starrfield <https://orcid.org/0000-0002-1359-6312>

References

- Amari, S., Gao, X., Nittler, L. R., et al. 2001, *ApJ*, 551, 1065
 Amari, S., Zinner, E., & Gallino, R. 2014, *GeCoA*, 133, 479
 Anders, E., & Zinner, E. 1993, *Metic*, 28, 490
 Bennett, M. B., Wrede, C., Brown, B. A., et al. 2016, *PhRvL*, 116, 102502
 Bose, M., & Starrfield, S. 2019, *ApJ*, 873, 14
 Brown, B. A., Richter, W. A., & Wrede, C. 2014, *PhRvC*, 89, 062801
 Budner, T., Friedman, M., Wrede, C., et al. 2022, *PhRvL*, 128, 182701
 Cameron, A. G. W. 1973, in *Interstellar Grains in Museums?*, ed. J. M. Greenberg & H. C. Van De Hulst (Berlin: Springer), 545

- Chen, H.-L., Woods, T. E., Yungelson, L. R., et al. 2019, *MNRAS*, **490**, 1678
- Chomiuk, L., Metzger, B. D., & Shen, K. J. 2021, *ARA&A*, **59**, 391
- Clayton, R. N., Grossman, L., & Mayeda, T. K. 1973, *Sci*, **182**, 485
- Cover, T. M., & Thomas, J. A. 2006, *Elements of Information Theory* (New York: Wiley)
- Downen, L., Iliadis, C., Champagne, A., et al. 2022, *ApJ*, **928**, 128
- Downen, L. N., Iliadis, C., Champagne, A. E., et al. 2022, *PhRvC*, **105**, 055804
- Downen, L. N., Iliadis, C., José, J., & Starrfield, S. 2013, *ApJ*, **762**, 105
- Endt, P. 1990, *NuPhA*, **521**, 1
- Fallis, J., Parikh, A., Bertone, P. F., et al. 2013, *PhRvC*, **88**, 045801
- Fuller, G. M., Fowler, W. A., & Newman, M. J. 1982, *ApJS*, **48**, 279
- Gehrz, R., Truran, J., Williams, R., & Starrfield, S. 1998, *PASP*, **110**, 3
- Gehrz, R. D. 2008, *Classical Novae*, Vol. 43 (2nd ed.; Cambridge: Cambridge Univ. Press), 167
- Gillespie, S. A., Parikh, A., Barton, C. J., et al. 2017, *PhRvC*, **96**, 025801
- Gyngard, F., Zinner, E., Nittler, L. R., et al. 2010, *ApJ*, **717**, 107
- Haenecour, P., Howe, J. Y., Zega, T. J., et al. 2019, *NatAs*, **3**, 626
- Hoppe, P., Leitner, J., Kodolányi, J., Borrmann, S., & Jones, A. P. 2022, *NatAs*, **6**, 1027
- Iliadis, C., Champagne, A., José, J., Starrfield, S., & Tupper, P. 2002, *ApJS*, **142**, 105
- Iliadis, C., Downen, L. N., José, J., Nittler, L. R., & Starrfield, S. 2018, *ApJ*, **855**, 76
- Iliadis, C., Longland, R., Champagne, A., Coc, A., & Fitzgerald, R. 2010, *NuPhA*, **841**, 31
- Iliadis, C., Longland, R., Coc, A., Timmes, F. X., & Champagne, A. E. 2015, *JPhG*, **42**, 034007
- Irvine, D., Chen, A. A., Parikh, A., et al. 2013, *PhRvC*, **88**, 055803
- José, J. 2016, *Stellar Explosions: Hydrodynamics and Nucleosynthesis* (Boca Raton, FL: CRC Press)
- José, J., Coc, A., & Hernanz, M. 2001, *ApJ*, **560**, 897
- José, J., & Hernanz, M. 2007, *M&PS*, **42**, 1135
- José, J., Hernanz, M., Amari, S., Lodders, K., & Zinner, E. 2004, *ApJ*, **612**, 414
- José, J., & Shore, S. 2008, *Classical Novae*, Vol. 43 (2nd ed.; Cambridge: Cambridge Univ. Press), 121
- Kamil, M., Triambak, S., Ball, G. C., et al. 2022, *PhRvC*, **105**, 055805
- Kankainen, A., Woods, P., Schatz, H., et al. 2017, *PhLB*, **769**, 549
- Koning, A., Hilaire, S., & Goriely, S. 2023, *EPJA*, **59**, 131
- Leitner, J., Kodolányi, J., Hoppe, P., & Floss, C. 2012, *ApJ*, **754**, L41
- Linfoot, E. H. 1957, *Information and Control*, **1**, 85
- Liu, N., Nittler, L. R., Alexander, C. M. O., et al. 2016, *ApJ*, **820**, 140
- Lodders, K. 2021, *SSRv*, **217**, 44
- Longland, R. 2012, *A&A*, **548**, A30
- Longland, R., Iliadis, C., Champagne, A., et al. 2010, *NuPhA*, **841**, 1
- Lovely, M., Lennarz, A., Connolly, D., et al. 2021, *PhRvC*, **103**, 055801
- Nabi, J.-U., & Klappdor-Kleingrothaus, H. 1999, *ADNDT*, **71**, 149
- Nguyen, A. N., & Messenger, S. 2014, *ApJ*, **784**, 149
- Nittler, L. R., & Ciesla, F. 2016, *ARA&A*, **54**, 53
- Nittler, L. R., & Hoppe, P. 2005, *ApJ*, **631**, L89
- Oda, T., Hino, M., Muto, K., Takahara, M., & Sato, K. 1994, *ADNDT*, **56**, 231
- Parikh, A., Wimmer, K., Faestermann, T., et al. 2011, *PhRvC*, **83**, 045806
- Parikh, A., Wimmer, K., Faestermann, T., et al. 2014, *PhLB*, **737**, 314
- Richter, W. A., Brown, B. A., Longland, R., et al. 2020, *PhRvC*, **102**, 025801
- Ritossa, C., Garcia-Berro, E., Iben, & Icko, J. 1996, *ApJ*, **460**, 489
- Sallaska, A. L., Iliadis, C., Champagne, A. E., et al. 2013, *ApJS*, **207**, 18
- Schulte, J., Bose, M., Young, P. A., & Vance, G. S. 2021, *ApJ*, **908**, 38
- Setoodehnia, K., Chen, A. A., Chen, J., et al. 2020, *PhRvC*, **102**, 045806
- Setoodehnia, K., Kelley, J. H., Marshall, C., Portillo Chaves, F., & Longland, R. 2019, *PhRvC*, **99**, 055812
- Starrfield, S., Bose, M., Iliadis, C., et al. 2020, *ApJ*, **895**, 70
- Starrfield, S., Bose, M., Iliadis, C., et al. 2024, *ApJ*, **962**, 191
- Starrfield, S., Iliadis, C., & Hix, W. R. 2008, *Classical Novae*, Vol. 43 (2nd ed.; Cambridge: Cambridge Univ. Press), 77
- van Raai, M. A., Lugaro, M., Karakas, A. I., & Iliadis, C. 2008, *A&A*, **478**, 521
- Wrede, C. 2014, *AIPA*, **4**, 041004
- Zinner, E. 2014, in *Treatise on Geochemistry*, ed. H. D. Holland & K. K. Turekian (2nd ed.; Amsterdam: Elsevier), 181